High-fidelity modelling of thermal stress for additive manufacturing by linking thermal-fluid and mechanical models

Fan Chen [a], Wentao Yan [a,b,*]

[a] Department of Mechanical Engineering, National University of Singapore, 117575, Singapore
[b] NUS Research Institute (NUSRI), Suzhou, Jiangsu 215123, China

HIGHLIGHTS

- Modelling thermal stress in AM using temperature profile from thermal-fluid model.
- Rough surfaces and internal voids are incorporated.
- Thermal stress concentrations due to voids and rough surfaces are revealed.
- Simulation results of thermal stress can rationally explain the cracks in experiments.

GRAPHICAL ABSTRACT
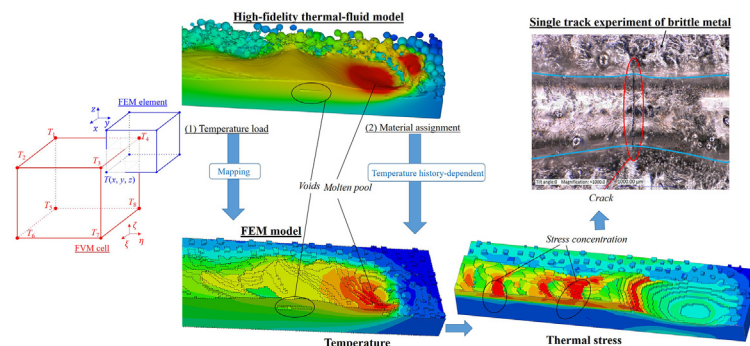
ARTICLE INFO

ABSTRACT

The prediction of thermal stress and distortion is a prerequisite for high-quality additive manufacturing (AM). The widely applied thermo-mechanical model using the finite element method (FEM) leaves much to be improved due to their oversimplifications on material deposition, molten pool flow, etc. In this study, a high-fidelity modelling approach by linking the thermal-fluid (computational fluid dynamics, CFD) and mechanical models (named as CFD-FEM model) is developed to predict the thermal stress for AM taking into account the influences of thermal-fluid flow. Profiting from the precise temperature profiles and melt track geometry extracted from the thermal-fluid model as well as the remarkable flexibility of the quiet element method of FEM, this work aims at simulating the thermal stress distribution by involving physical changes in the AM process, e.g., melting and solidification of powder particles, molten pool evolution and inter-track inter-layer re-melting. Unlike the conventional thermo-mechanical analysis, in this approach, thermal stress calculation is purely based on a mechanical model where the thermal loads are applied by using a linear interpolation function to spatially and temporally map the temperature values from the thermal-fluid model's cell centres into the FEM element nodes. With the proposed approach, the thermal stress evolution in the AM process of single track, multiple tracks and multiple layers are simulated, where the rough surfaces and internal voids can be well incorporated. Moreover, a conventional thermo-mechanical simulation of two tracks with predefined track geometry is conducted for cross comparison. Finally, the simulated thermal stress distribution can rationally explain the crack distribution observed in the experiments.

© 2020 The Author(s). Published by Elsevier Ltd. This is an open access article under the CC BY license (http://creativecommons.org/licenses/by/4.0/).

1. Introduction

Additive manufacturing (AM) is a promising technology capable of producing complex-shaped parts without the need for special tooling

* Corresponding author at: Department of Mechanical Engineering, National University of Singapore, 117575, Singapore.
E-mail address: mpeyanw@nus.edu.sg (W. Yan).

[1,2]. However, the heat source scanning usually induces steep temperature gradients, and hence causes high thermal stress. Such high thermal stress would cause lots of defects, e.g. cracks, delamination, shrinkage, warpage etc. [3–8], and has been considered to be a bottleneck problem. The effects of different processing parameters on the thermal stress of the final products have been investigated experimentally and numerically by a number of scholars and researchers around the world.

Experimentally tracing the thermal stress evolution during the melting process is inexpedient under current circumstances due to the high local temperature and the fast heating/cooling rate. Post-process experimental characterizations of thermal stress, e.g., hole-drilling method [9,10], Neutron diffraction [11,12], and x-ray diffraction [13], can provide some useful information. However, the parameter optimization via trial-and-error experiments and post-process characterization is quite expensive given the large number of processing parameters, and the spatial distribution of thermal stress, temperature and absorbed energy is also difficult to experimentally measure.

Companies and scientists have devoted a lot of money and efforts in developing efficient numerical tools to analyse the thermal stress and distortion in the large scale, e.g., 3DSIM [14] acquired by ANSYS, 3DEXPERIENCE Make platform [15,16] acquired by Dassault Systèmes, and Pan Computing LLC [17,18] acquired by Autodesk. Most of the current softwares use the inherent strain model to ensure the computation efficiency, which simplifies the melting-solidification process along scan paths to a pure mechanical simulation of sequentially accumulating representative elements of single tracks with inherent strains. Liang et al. [19,20] put a lot of efforts in constructing the inherent strain model to predict residual distortion. Agglomeration approaches is also commonly applied for the part-scale modelling of the AM products, where a large computational layer is constructed by lumping many sub-layers together [21]. However, there is still much room for improvement of the applicability and predictability of these simulations, which are based on assumptions, theoretical estimation or thermal and geometrical simplifications.

Many researchers attempted to improve the predictability of FEM simulation by considering the heating, melting and solidification factors but omitted the effects of thermal-fluid flow. In most cases of thermo-mechanical simulation, the heat conduction equations are solved directly on the FEM model and the entire track or layer is set to be active at the beginning of the melting process, regardless of the powder melting process and the track forming procedure [22–26] [27,28]. However, due to the sequentiality of the material deposition process, the elements being deposited should not be affected by the prospectively deposited elements, and the prospectively deposited elements should be either deactivated or suppressed [29–32]. Cheon et al. [33,34] analysed the thermal-metallurgical-mechanical behaviour of the welding process based on a CFD-FEM framework [35] with the consideration of the phase dependent thermal strains; the mechanical history reset of the liquid state was however not considered. Bailey et al. [36] incorporated the influence of the molten pool, track re-melting and layer formation process into laser direct deposition modelling by deactivating the upper tracks and liquid state elements. Bailey's model was validated by experiments in part scale, but it cannot locally reveal the stress concentration on the individual tracks as the cross section of all the deposited tracks are simplified to be smooth and uniform without defects. The defects generated during the manufacturing process, like high surface roughness and porosity, can potentially change the stress distribution or perhaps cause local stress concentration. Foteinopoulos et al. [37] involved the factors of the defects in the FEM by inducing the volumetric fraction of porosity, to simplify the tracks into uniform-shaped blocks. However, the involvement of the small defects in thermo-mechanical simulation seems impractical due to the intricate track geometry approximation.

The inactive element method [38–41] is well-known as one of the commonly applied numerical approaches to simulate the material

deposition process. Huang [42] et al. applied the progressive element birth to simulate the material deposition of the wire and arc additive manufacturing. The inactive elements are attributed with ordinary material properties but excluded from the structural stiffness at the beginning of the calculation [41], so that the track forming procedure can be represented by sequentially activating the designated element sets. However, since the temperature of the interface nodes is obtained by the interpolation between active and inactive elements, the interface nodal temperature will be lower than the desired value as the temperature for an inactive element is set to be zero by default(shown in Appendix Fig. 14). Such problem had been described in detail by Michaleris et al. [43] who built a 1D model to analyse the temperature calculation scheme on the node shared by two elements, active and inactive respectively. For the pure mechanical analysis proposed in this study, the heat transfer mechanism is superseded by the direct loading of the temperature, thus the inactive element method is not applicable since the temperature compensation for the interface nodes is quite knotty.

In this work, we develop a high-fidelity modelling approach for thermal stress by mapping the temperature profiles from the thermal-fluid model [8,44] to the mechanical model, to ensure the accuracy of the temperature profile and to incorporate the realistic geometry including both rough surfaces and internal pores and voids. As illustrated in Fig. 1, the coupling of the CFD and FEM is one-way, and the temperature profiles extracted from the CFD model function in the FEM model in two aspects, i.e., temperature load and material assignment. In the mechanical model using the FEM, the quiet element method (QEM) [45,46] is employed to incorporate the complex changes of geometry due to melting/re-melting, solidification, and molten pool flow. The thermal-fluid model, temperature mapping scheme, thermal stress model and parameter settings are described in Section 2, the conventional thermo-mechanical model is built for cross comparison in Section 3, and the simulation results and discussion are in Section 4.

2. Model construction

2.1. Thermal-fluid model

The thermal-fluid simulation that resolves individual powder particles is by the CFD software FLOW-3D and has been experimentally validated to be accurate in a variety of AM cases [8,44,47,48]. In the thermal-fluid simulation, the melted material flow is assumed to be incompressible laminar flow. The governing equations are mass continuity, momentum conservation and energy conservation given in Eq. 1 [8].

$$
\begin{cases}
\nabla \cdot (\rho \boldsymbol{v}) = 0, \\
\dfrac{\partial}{\partial t}(\rho \boldsymbol{v}) + \nabla \cdot (\rho \boldsymbol{v} \otimes \boldsymbol{v}) = \nabla \cdot (\mu \nabla \boldsymbol{v}) - \nabla p + \rho \boldsymbol{g} + \boldsymbol{f_B}, \\
hskip - 150 \dfrac{\partial}{\partial t}(\rho h) + \nabla \cdot (\rho \boldsymbol{v} h) = q + \nabla \cdot (k \nabla T),
\end{cases}
\tag{1}
$$

where $\boldsymbol{v}$ is the velocity vector, μ is the viscosity, p is the pressure, k is the thermal conductivity, and T is the temperature. In the energy conservation equation, h represents the specific enthalpy calculated by $h = cT + (1 - f_s)L$, where c, f_s and L denote the specific heat, solid fraction and latent heat of melting, respectively, thus the latent is linearly released with the temperature. The momentum equation incorporates gravity ($\boldsymbol{g}$), buoyancy ($\boldsymbol{f_B}$, Boussinesq approximation), and viscosity (μ). The boundary conditions for the momentum conservation equation incorporate surface tension, recoil pressure and Marangoni forces, and the thermal boundary conditions incorporate the surface radiation and energy loss by evaporation.

The Volume of Fluid (VOF) method [49] is applied to re-construct the free surface at each time increment, given in Eq. 2.
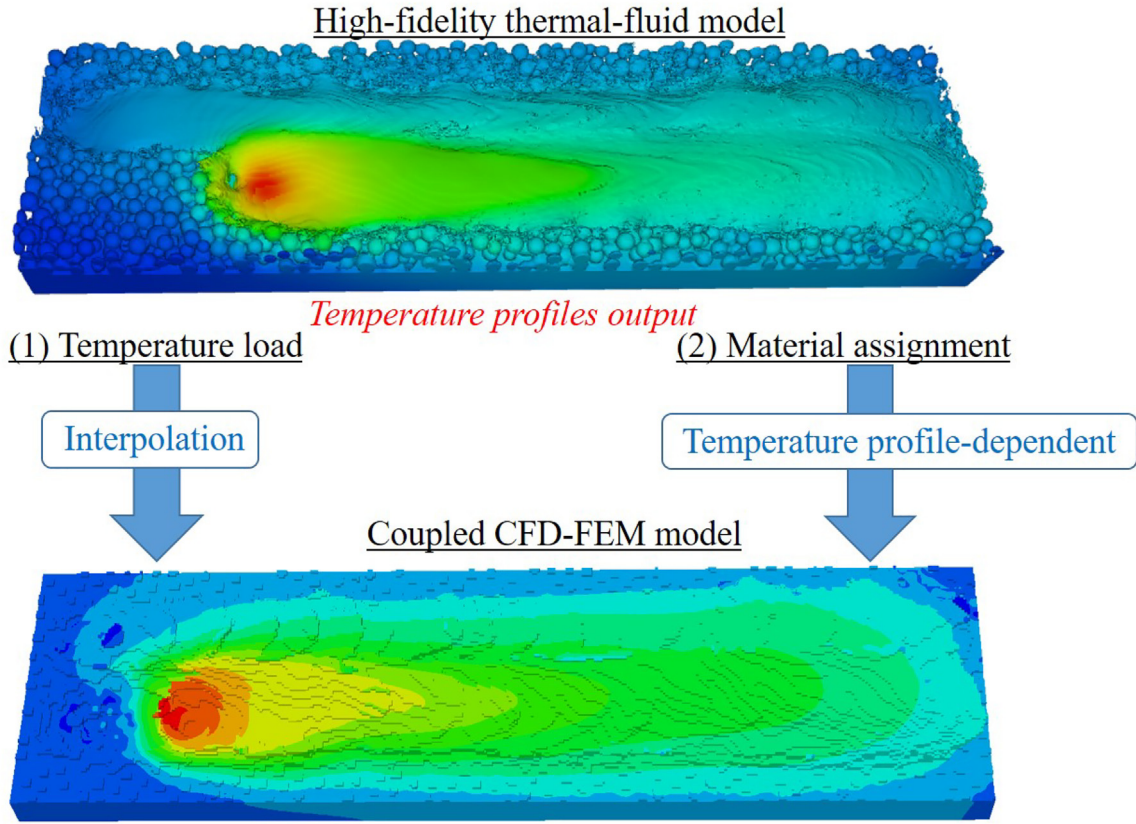
Fig. 1. Schematic of linking thermal-fluid and mechanical models, consisting of (1) mapping the temperature profiles from the thermal-fluid model to the mechanical model, and (2) assigning the corresponding material states.

$$\frac{\partial F}{\partial t} + \nabla \cdot (F\boldsymbol{v}) = 0. \tag{2}$$

where F denotes the fluid fraction. Further details about the model can be referred to [8,47].

2.2. Thermal stress calculation in the FEM model

As the coupling between CFD and FEM is one-way, the thermal-fluid simulation is entirely independent of the FEM computation and the temperature history can be imposed directly onto the FEM model. Therefore, no transient heat transfer analysis is involved and the FEM simulation is a pure mechanical analysis. Due to the lack of reliable material parameters for the thermal-elastic-plastic constitutive mode, we hereby assume the material to be linear elastic. The governing equations applied to correlate the thermal strain, local temperature and thermal stress are shown in Eq. 3 [50,51]..

$$\begin{cases} \varepsilon^{th} = \alpha\left(T, f_\beta\right)\left(T - T^0\right) - \alpha\left(T^I, f_\beta^I\right)\left(T^I - T^0\right) \\ \boldsymbol{\sigma} = \boldsymbol{D}\boldsymbol{\varepsilon} \end{cases} \tag{3}$$

where $\alpha(T, f_\beta)$ represents the thermal expansion coefficient, T is the current temperature, T^I is the initial temperature, f_β represents the current material state, f_β^I represents the initial material state, and T^0 represents the reference temperature for the thermal expansion coefficient. Additionally, $\boldsymbol{\sigma}$ denotes the stress matrix, $\boldsymbol{D}$ denotes the elasticity tensor, and $\boldsymbol{\varepsilon}$ is the elastic strain matrix.
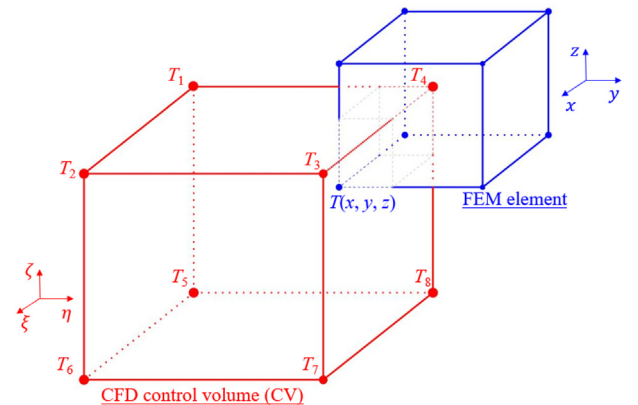
2.3. Mapping and interpolation

The temperature profiles are loaded based on the 3D interpolation that maps the temperature stored in the centre of Eulerian control volume (CV) of the CFD model onto the node of the Lagrangian element of the FEM model, as shown in Fig. 2. Given the Eulerian structural mesh in the CFD model, we utilize the shape function of the brick element in the FEM as the interpolation function, given as Eq. 4 [52].

$$\begin{cases} T = \sum_{i=1}^{8} N_i(\xi, \eta, \zeta) T_i \\ N_i(\xi, \eta, \zeta) = \frac{1}{8}(1 - \xi\xi_i)(1 - \eta\eta_i)(1 - \zeta\zeta_i), i = 1, 2, \ldots, 8 \end{cases} \tag{4}$$

where ξ, η and ζ are the local coordinates in the CFD coordinate system, ξ_i, η_i and ζ_i are the natural coordinates of the CV centres surrounding the FEM node and $T_i(\xi, \eta, \zeta), i = 1, 2, \ldots, 8$ denote the temperature values of 8 CV centers surrounding the element node, respectively. Moreover, T is

Fig. 2. Schematic of the temperature interpolation between the CFD CV centres and FEM nodes.

the interpolated temperature value for the FEM node inside CV, and N_i (ξ, η, ζ) is the interpolation function. It should be noted that this mapping scheme including the interpolation function is generally applicable to any 3D FEM element shapes, and the 8-node linear brick element (C3D8R) is used in the FEM model of this study. After obtaining the temperature $T(t_1)$ and $T(t_2)$ by Eq. 4 on two adjacent instants t_1 and t_2 specified in CFD simulation, the temperature value $T(t')$ in between $(t_1 \leq t' \leq t_2)$ can be approximated by the 1D interpolation, given by Eq. 5.

$$T(t') = T(t_1) + \frac{T(t_2) - T(t_1)}{t_2 - t_1}(t' - t_1) \qquad (5)$$

The time step size in the FEM model, $\Delta t'$, is different from the data output time interval of the CFD model, Δt. To fully exploit the CFD temperature profiles output, $\Delta t'$ is smaller than Δt to allow a temperature interpolation between any two time-adjacent CFD temperature profiles.

2.4. Material state

The QEM remedies the shortcomings of the inactive element method in simulating the evolution of the molten pool and the remelting of previous tracks. The idea of the QEM is to assign null material properties to non-deposited elements whose presence should not affect the deposited elements, as Fig. 3 shows. In the QEM, the material properties of the elements should change with the corresponding state, i.e., air, liquid or solid. As illustrated in Fig. 4, the elements' material states transfer to the liquid state from the solid state where the powders or the previous tracks and substrate are melted; elements transfer from the liquid state to the solid state due to solidification. Besides, with the molten pool evolution, the elements material states may transfer from liquid state to the air state when the liquid flows away, or from the air state to the liquid state when it flows in. It should be noted that there is no state transfer between solid and gas. In addition, since the effect of the unmelted powders on the stress distribution can be ignored, the unmelted powders are treated to be the air state.
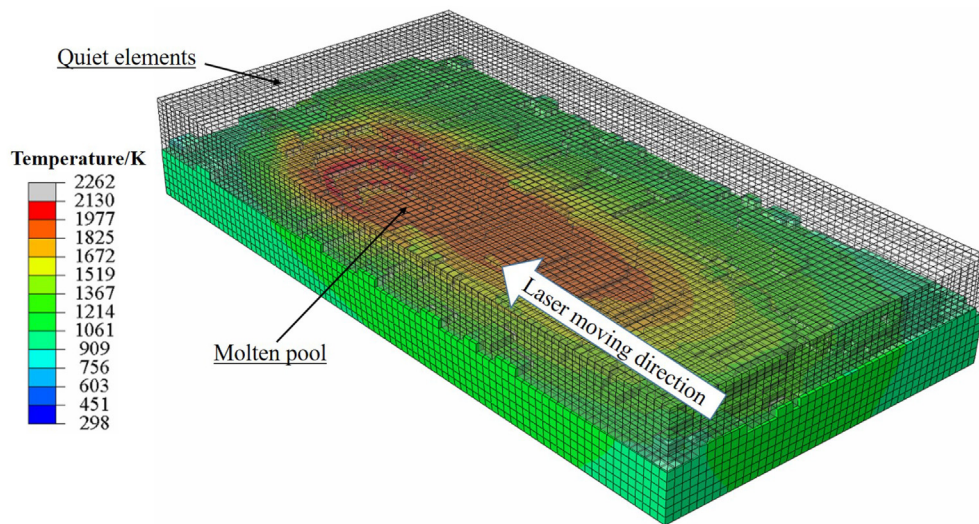

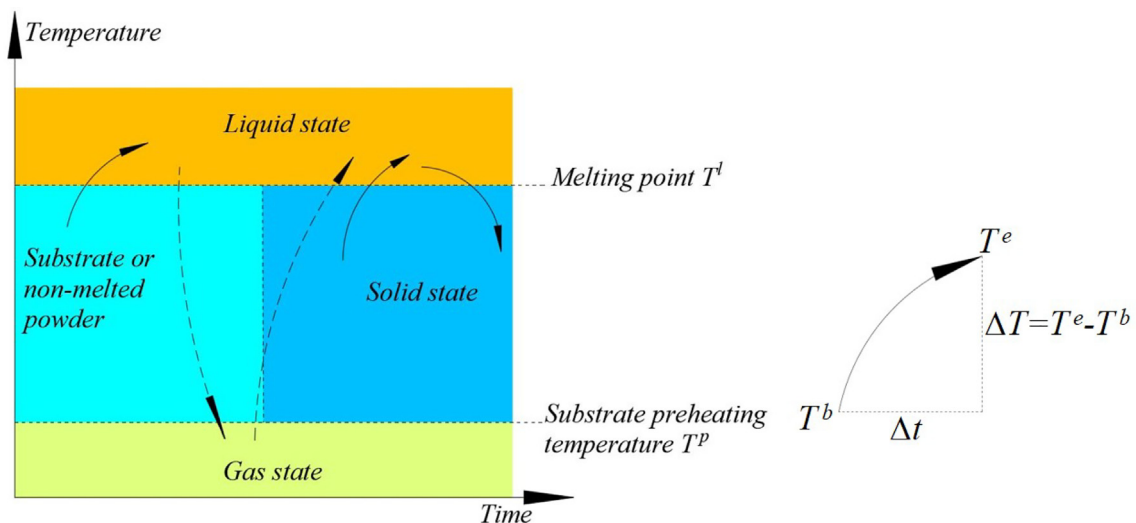**Fig. 3.** Schematic of the quiet element model.

Fig. 4. The material state changes during the melting and solidification process, including ① the substrate and powders are molten into liquid metal, ② the liquid material flows away and the state transfers to air and ③ the state transfers to liquid when liquid flows in, ④ the solidified material may be re-melted into liquid, and ⑤ the liquid metal solidifies.

Therefore, the material state of each element depends on not only the current temperature but also the temperature history. Within a time increment Δt, the interpolated temperature value for a node is T^b at the beginning and becomes T^e after Δt, so the temperature change is $\Delta T = T^e - T^b$. The melting point (the liquidus temperature for an alloy) and initial temperature (i.e., the preheating temperature) are constant and denoted by T^l and T^p, respectively, and then the temperature criteria for the material state transformation are defined as follows:

• melting: if $\Delta T > 0$, $T^b < T^l$ and $T^e > T^l$, the node undergoes melting process and the material state for the node changes from solid to liquid;

• solidification: if $\Delta T < 0$, $T^b > T^l$ and $T^e < T^l$, the node is solidifying underway and the material state changes from liquid to solid;

• if $T^e < T^p$, it is the environmental temperature and the material state is set as air.

2.5. Material parameters

The material is Ti-6Al-4 V. For the thermal-fluid simulation, the material properties are listed in Table 1 [8]. The simulation case is the electron beam melting process under the vacuum environment where no
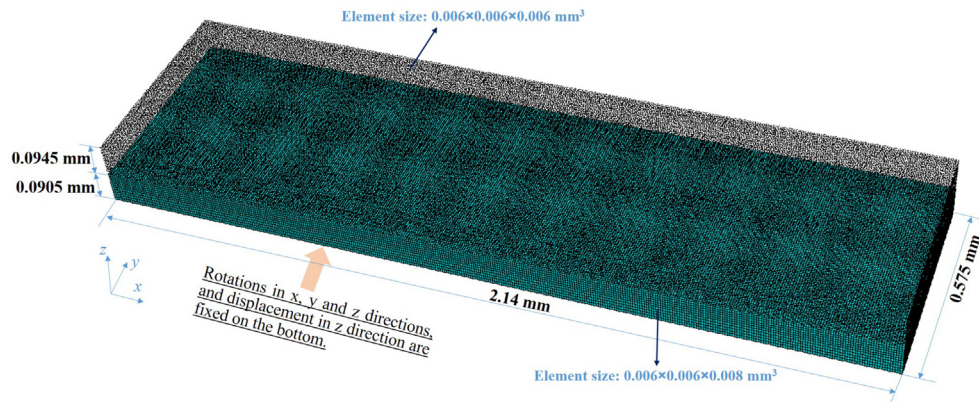
gas phase needs to be considered. More details for the thermal-fluid modelling are given in references [8, 44, 47].

In the FEM model, three material states, i.e. solid, liquid and air, change depending on the temperature profile as shown in Fig. 4. The material properties for different states are listed in Table 2, in which the solidus elements are assigned with the material properties of Ti-6Al-4 V. In practise, the quiet elements still count for parts of the global stiffness but do not affect the solidus phase if setting the stiffness of all the quiet elements as zero. Considering the convergence, assigning a zero Young's modulus to the air and molten liquid metal will lead to serious element deformation near the interface with the solid phases. Therefore, the air and liquid elements are assigned with a small Young's modulus 1×10^4 Pa and Poisson ratio 1×10^{-3}, which are large enough to avoid numerical divergence for the non-solid elements but small enough to be" quiet" for the stress analysis. It has been tested that the Poisson ratio values assigned to the air and liquid states do not make difference to the thermal stress distribution of the solid if the Young's modulus is sufficiently small.

2.6. Simulation cases and computational cost

It is worth mentioning that our modelling approach is applicable to a wide variety of fusion-based manufacturing processes, e.g., selective laser melting, electron beam melting, directed energy deposition, and wire arc additive manufacturing. Here we conduct an example case of electron beam melting. We run a simulation case of 2-layer 2-track electron beam melting process. The electron beam diameter, scanning speed, power and layer thickness are 0.4 mm, 0.5 m/s, 60 W and 0.05 mm, respectively. The preheating temperature is 873 K. In the case, the geometrical features, e.g., rough surfaces and voids, are incorporated, and the re-melting of the previously deposited track and layer is also incorporated, which is representative of such AM processes. The temperature profiles are output from the thermal-fluid model in an interval of 0.0002 s, while the time step size of the FEM model is set to be 0.0001 ~ 0.0002 s. The mesh size in the thermal-fluid model is 0.005 mm, as detailed in our previous work [8]. As Fig. 5 shows, in the FEM model, there are 922,752 elements and 969,612 nodes; the element dimension is $0.006 \times 0.006 \times 0.008$ mm^3 in the substrate and $0.006 \times 0.006 \times 0.006$ mm^3 in the region above the substrate. A mesh convergence test has been conducted to exclude mesh sensitivity.

The computation time is around 700 h for the thermal-fluid simulation on an Intel Core i7–2600 CPU (4 cores, 8 threads and 3.40 GHz for the Processor Base Frequency) and 330 h for the FEM simulation on an Intel X5650 CPU (6 cores, 12 threads and 2.66 GHz for the Processor Base Frequency). The computational cost for FEM model can be greatly reduced by optimizing the temperature loading scheme, which is under further investigation and will be introduced in future publications.

Table 1
The material parameters for CFD simulation.

Material property	Value
Specific heat (c_p)	872 J/(K · kg)
Latent heat of melting (L_m)	2.86×10^5 J/kg
Latent heat of evaporation(L_v)	9.7×10^6 J/kg
Density(ρ_l)	4000 kg/m^3
Surface radiation coefficient (α_b)	0.4
Surface tension coefficient(σ)	1.68 N/m
Viscosity (μ)	0.005 Pa · s
Solidus thermal conductivity (k)	16 W/(m · K)
Liquidus thermal conductivity (k)	32 W/(m · K)
Temperature sensitivity of surface tension coefficient (σ_s^T)	0.00026
Solidus temperature (T^s)	1878 K
Liquidus temperature (T^l)	1928 K

Table 2
Material parameters for different material states in the FEM model.

Material states	Young's modulus (Pa)	Poisson ratio	Thermal expansion coefficient(1/K)
Solid	1.32×10^{11}	0.31	9.2×10^{-6}
Liquid	1×10^4	0.001	9.2×10^{-6}
Air	1×10^4	0.001	0

Fig. 5. Geometry dimension, meshing and boundary conditions of the FEM model.

3. Thermo-mechanical model for cross comparison

A thermo-mechanical simulation is conducted for cross comparison with the CFD-FEM simulation. To ensure a fair cross-comparison, we constructed a curved track shape, mimicking that from the thermal-fluid simulation as shown in Fig. 6. Since the fine geometrical features

of the rough surface can be problematic for the FEM model to generate mesh and to apply the heat source, the surfaces of the tracks have to be modified to be smooth, as shown in Fig. 6 (b). The mesh contains 209,304 hexahedral elements and 234,866 nodes and the computational cost is about 200 h on an Intel X5650 CPU. The elements type is the 8-node thermally coupled brick element (C3D8T). The scanning
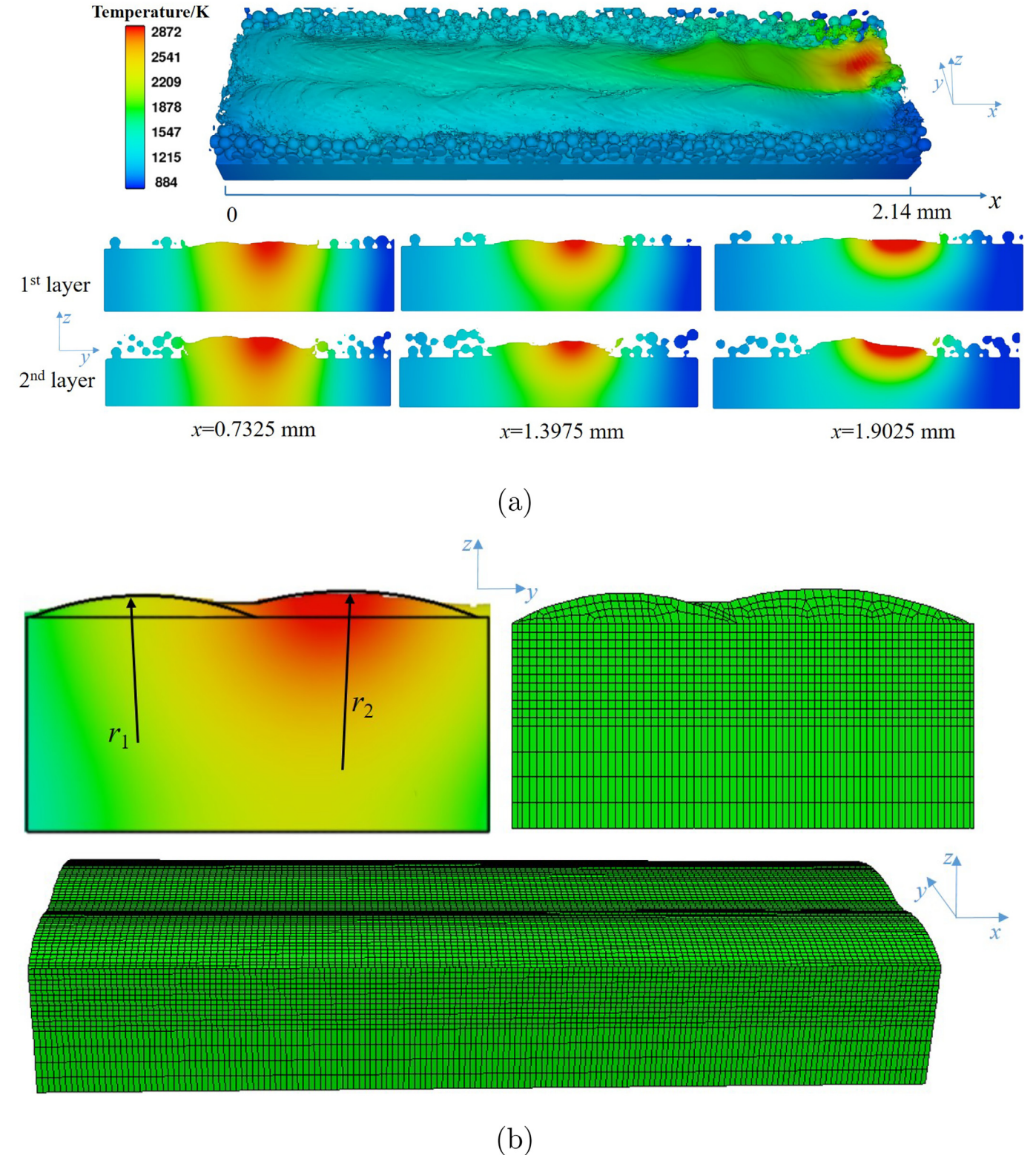

(a)

(b)

Fig. 6. (a) Thermal-fluid simulation results. (b) The geometrical shape of the thermo-mechanical model mimicking the middle segment of the first layer in the thermal-fluid model.

parameters and the material properties are identical to those listed in section 2.5, and the input energy obeys Gaussian distribution as given in Eq. 6 [44],

$$q(x,y) = Q \times \eta \times \left[\frac{C}{\pi R_b^2} \exp\left(- \frac{C \cdot \left[(x-x_b)^2 + (y-y_b)^2 \right]}{R_b^2} \right) \right] \qquad (6)$$

where no electron penetration has been considered because the element size is larger than the maximum penetration depth of the electron beam. In Eq.6, C is the concentration coefficient, R_b is the electron beam radius, (x_b, y_b) represents the coordinate of the electron beam centre, and Q is the electron beam power and η is the energy absorptivity. $Q \times \eta$ is equal to the absorbed power applied in thermal-fluid simulation. More details for Eq. 6 are available in reference [44, 47].

4. Results and discussion

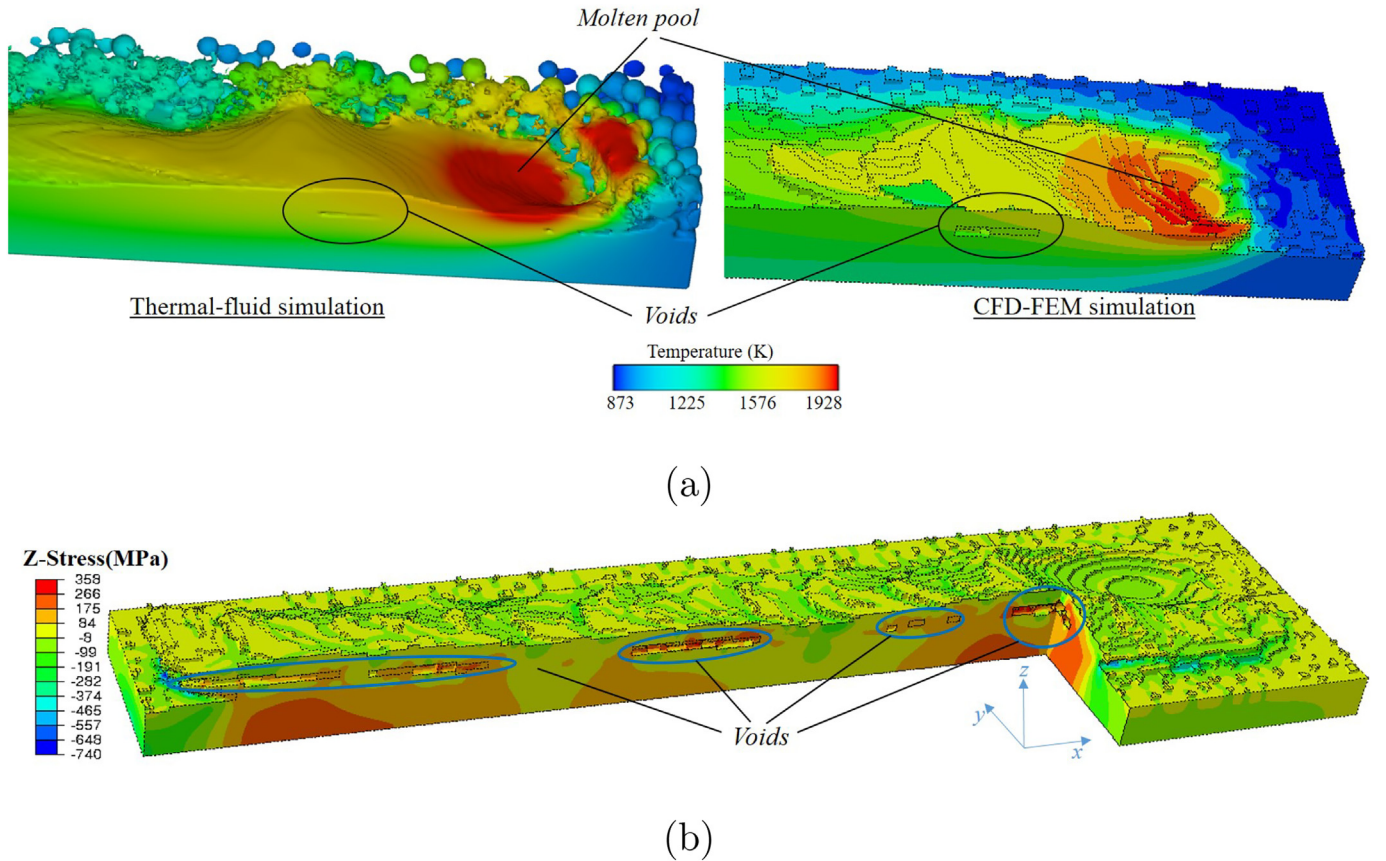### 4.1. Temperature distribution and morphology

Fig. 7 (a) provides two sectional views partially showing the voids, rough surface and molten pool morphology of the mechanical and thermal-fluid simulation results, while more detailed comparative snapshots of the FEM simulation results and thermal-fluid simulation results are shown in the Appendix Fig. 15. The powders and the liquid state elements that can hardly affect the stress distribution are not visualized in the FEM results. Thus the molten pool shape looks slightly different, but the shape of the formed track is quite similar. The results of

the geometrical features and the temperature distribution of the FEM and CFD models show a good agreement, except the terraced surface caused by the voxel mesh. It is worth mentioning that the void has also been mapped, which causes the stress concentration especially in the z direction, as shown in Fig. 7 (b). The fidelity of the FEM temperature distribution can be improved by refining the mesh and reducing the time step size of the FEM simulation.

4.2. Stress distribution

The temperature gradient along the x-y plane in the cross section of the 1st layer is plotted at the end of the fabrication of the 1st layer ($t = 0.008$ s) as shown in Fig. 8. The temperature gradient in the header part of the track after heating is larger than that of the middle region, which will cause a higher level of compression as displayed in Appendix Fig. 16.

As the simulated time interval for the two-track two-layer example is not long enough for the fully cooling down, we only observe the thermal stress history during the heating and cooling process. The stress curves are plotted based on the stress datum recorded on 7 designated nodes, which are located on the vertical line that passes through the center region of the first and third tracks, as illustrated in Fig. 9. Nodes A and B are inside the third track, node C is inside the third track but quite close to the top surface of the first track, node D is within the first track, and nodes E, F and G are within the substrate. Their corresponding stress component curves in x, y and z directions, respectively denoted as X-stress, Y-stress and Z-stress. The heat source scans over the observation region from $t_1' = 0.00155$ s to $t_2' = 0.00255$ s; during

Molten pool

Thermal-fluid simulation

Voids

CFD-FEM simulation

Temperature (K)

873   1225   1576   1928

(a)

Z-Stress(MPa)

359
266
175
84
-9
-99
-191
-282
-374
-465
-557
-648
-740

Voids

(b)

Fig. 7. (a) Comparison of the geometrical features and the temperature field between the simulation results of the coupled CFD-FEM model and thermal-fluid model. (b) Stress concentrations in z direction caused by the voids.
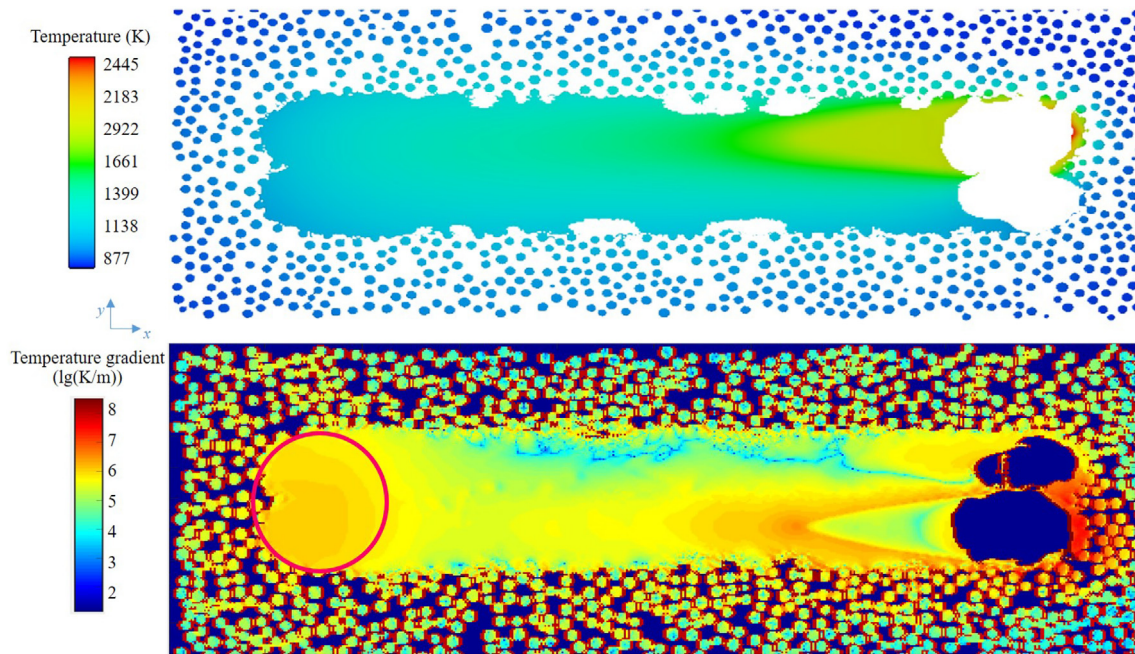
Fig. 8. Temperature and temperature gradient in the cross section of the 1st layer at $t = 0.008$ s along the x-y plane.

this period, the heated area around the molten pool tends to expand but is constrained by the surrounding cooler elements, thus the stress components of nodes D, E and F around the heated region are under compression, while the stresses for nodes A, B and C are 0 because the third track remains" quiet". Once material states of the nodes D and E change to the liquid at the moment the molten pool arrives, their stress components become 0, because the compressive stresses are totally released in the liquid state. In the melting of the second track (0.004 s~ 0.008 s), the heat source is away from the observation nodes, and the 1st-track shrinks in the x direction but under the expansion force along the Y direction from the heating of the 2nd-track. Therefore, as shown in Fig. 9, X-stress changes from compression to tension and Y-stress remains negative. Node G is relatively far from the heating area and still primarily affected by the material shrinkage.

As the 3rd-track is manufactured during 0.008 s~ 0.012 s, the 1st-track simultaneously experiences the re-melting treatment. From Fig. 9, the molten pool once more moves through the observation position with another layer of elements covering the 1st-track. Nodes A, B and C are inside the newly deposited track. Since the top surface can expand more easily than the inner region, the stress level of the inner node C is larger than that of node A located near the top surface. Meanwhile, as the heat source scans forward from the starting point, the tensile stress of nodes D, E and F will be counteracted by the expansion, then fully released to 0 due to re-melting and changes to compression again, but then immediately recovers to tension in the subsequent rapid cooling process. Node G is sufficiently far from the heating region and thus maintains a tensile stress, which even rises to a higher level after heating.

Note that compression stresses magnitude in some nodes are quite large, over 800 MPa for X-stress on the nodes A, B and C. It is because the thermo-elastic-plastic relationship is not considered and in reality, the Young's modulus is not a constant but becomes lower at high temperatures. The subsequent cooling-down pattern after $t_1' = 0.016$ s can not be observed based on the current outcome due to the simulation time limit. Yet the stress pattern on the upper layers can be hypothesized to be similar to the lower layers.

4.3. Comparison with the thermo-mechanical model

The comparison of the thermal stress and temperature distribution between the thermo-mechanical and coupled CFD-FEM simulation are shown in Fig. 10, where only the first layer is included. While the absorbed power $Q \times \eta$ applied for the thermo-mechanical and thermal-fluid model is equal, the peak temperature in the molten pool region of the thermo-mechanical simulation (4228 K) is much higher than the CFD-FEM simulation (2382 K) as the energy dissipation by evaporation is omitted in the thermo-mechanical simulation. From Fig. 10, the molten pool size is relatively small in the thermo-mechanical simulation, because the molten pool flow is not incorporated, particularly the Marangoni effect which usually enlarges the molten pool by enhancing convection. In the CFD-FEM modelling approach, the high-fidelity thermal-fluid simulation provides the physically-informed temperature profiles and authentic geometrical features for the mechanical simulation, while in the thermo-mechanical model, the heat source is directly applied on the predefined track surface.

From Fig. 10 (b), there are some stress concentration regions on the processed track of the CFD-FEM model, while the stress in the thermo-mechanical model is mostly released after the heating as the track surface is smooth. Furthermore, the three stress components in x, y and z directions, namely X-stress, Y-stress and Z-stress, are compared on nodes D, E and F in Fig. 11. As the meshes for these two simulations are different, the coordinates of the observation nodes D, E and F in the thermo-mechanical model cannot be selected identically but are as close as possible to those of the FEM-CFD model, as illustrated in Fig. 11 (a). When the molten pool arrives at the observation position, node D is inside molten pool, nodes E is located at the boundary of the molten pool and node F is below the molten pool. From the stress curves shown in Fig. 11 (b), node D of the thermo-mechanical model undertakes the higher molten pool peak temperature as well as the larger temperature gradient given the same temperature level in the cooling region, thereby the stress magnitude is higher than the CFD-FEM simulation, while on node F it is lower. With the consideration of the liquid state, the stress evolution for the CFD-FEM simulation is more sophisticated than the simplified
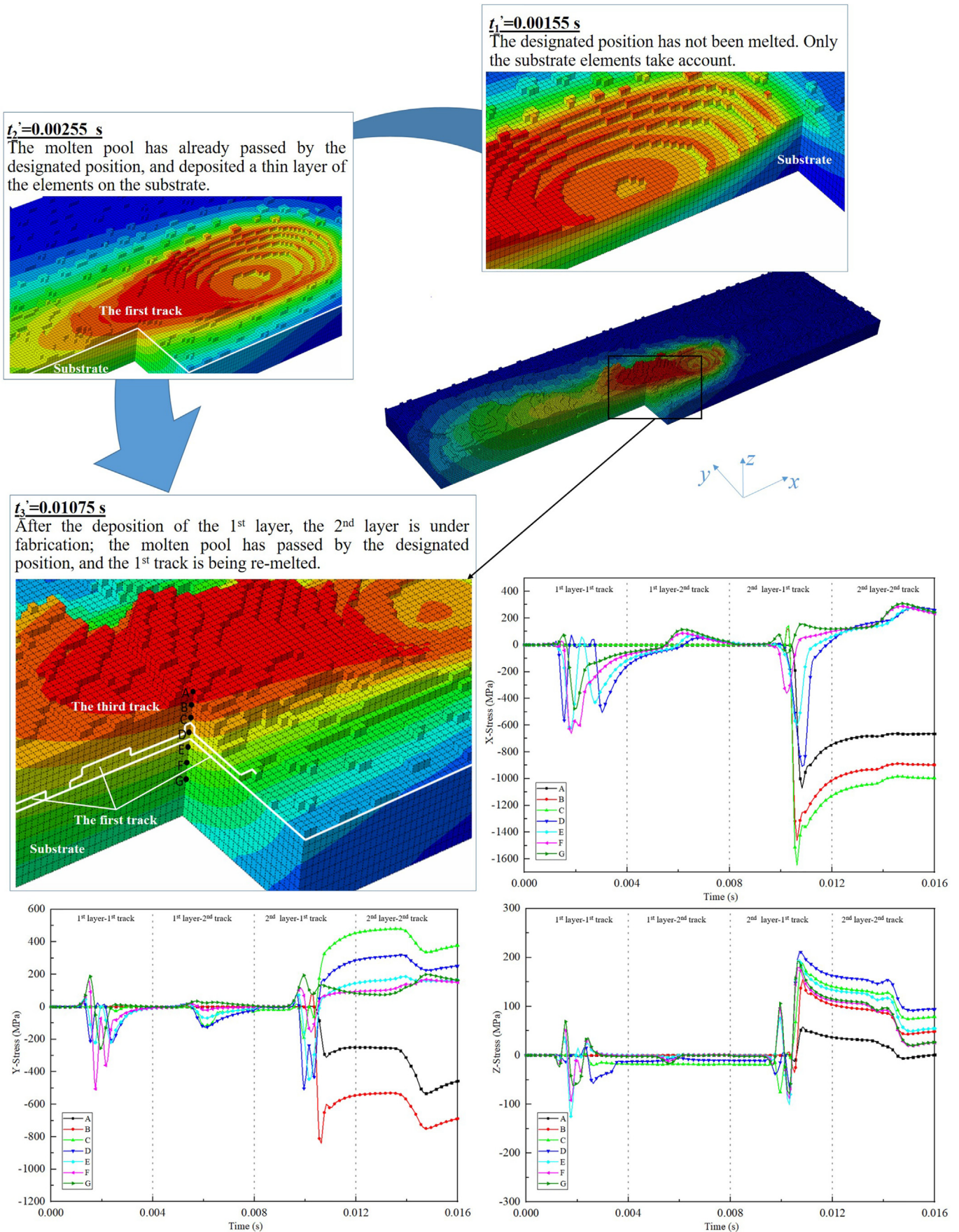
Fig. 9. The material deposition process specified at the observed position; the distribution of the observation nodes in different layers and their stress component curves in X, Y and Z directions.
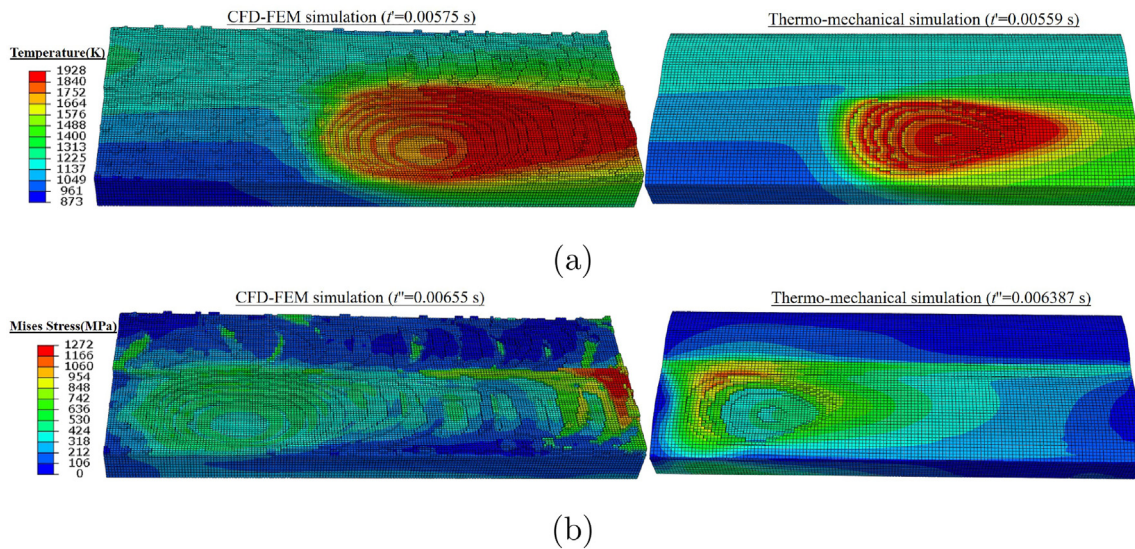
Fig. 10. The comparison of (a) the temperature and (b) stress distribution between the CFD-FEM and thermo-mechanical simulation.

thermo-mechanical simulation; at the moment that the molten pool scans over the observation nodes, the compressive stress on nodes D and E will be released to 0 in the CFD-FEM model, while in the thermo-mechanical model, the compression in the same region reaches the peak, as shown in Fig. 11 (b) and (c).

4.4. Example applications

We try to find the potential evidence for the mechanism of the crack generation or other forms of defects [53,54] using the proposed high-fidelity modelling. Normally, the deposited elements bear large compressive thermal stress in the heated region; with the heat source moving away, the elements starts to shrink. Thus, we focus on the cooling region where the residual stress concentration may occur. The snapshots revealing the evolution of the stress component in the x direction in the multiple-track simulation are displayed in Appendix Fig. 16 in chronological order. It reveals that $t' = 0.00915$ s, the first layer has almost cooled down and the overall X-stress component state in the middle region changes to be tensile, together with the emergence of many small stress concentration regions.

As shown in Fig. 12, the red color of the stress distribution highlights the tensile stress concentration regions where the cracks are more likely to occur. As shown in Fig. 12 (a), the single-track experiments by the SLM of the Fe-based metallic glass is conducted on Aconity Mini (Aconity GmbH, Germany) with the heat power 100 W, scanning speed 200 mm/s and the layer thickness of 100 m; the propagation orientation of the surface crack is perpendicular to the scanning path; such cracks are often caused by the large stress component along the scanning path; the stress (X component) concentration regions in the CFD-FEM simulation are distributed primarily around the edge of the surface's small wrinkles, which possibly explains the mechanism for crack generation vertical to the scanning path; it can be speculated that the long cracks vertical to the scanning path on the multiple tracks surface may be generated by the propagation of these small cracks. In the thermo-mechanical simulation, the X-stress is however distributed quite smoothly on the track surface, where no tensile stress concentration region can be found.

Moreover, the stress component distributions in y and z directions are shown in Fig. 12 (b) and (c), respectively. There is a long stress (Y component) concentration region along the inter-track gap, which may cause the cracks parallel to the scanning path direction. The stress

(Z component) concentration occurs mainly around the interface between different layers, especially in the regions around the voids, which may further lead to the delamination. It should be mentioned that we observe the Z-stress distribution at the instant when two layers are fully deposited so that the defects between two layers can be shown. As the X and Y stress components mainly concentrate on the layer surface, both of them are output at the instant when the 1st layer has been fully deposited and almost cooled down.

Furthermore, we compared the single track CFD-FEM simulation results with the experimental results by Vrancken et al. [55]. As shown in Fig. 13, the experimental cases conducted with different sets of laser power and scan speed are shown at different instants, i.e., t_1', t_2', t_3' and t_4'. At t_1', the laser reaches the left side; at t_2', the laser is in the middle of the track segment; at t_3', the laser just passes the observed region; at t_4', the laser passes far away, and cracking perpendicular to the track occurs. For the evolution of the X-stress from the CFD-FEM simulation, the track segment is under compression at t_3', so no cracks can be found in the experimental results. At t_4' when the laser passes far away and the track segment is further cooling down and shrinking, the X-stress becomes tensile, with these stress concentration regions perpendicular to the track, which rationally explains the cracks generation in the single track experiments. Moreover, our approach has also been applied in the investigation of high-density dislocations in additively manufactured copper [56]. The residual stress distribution achieved by the CFD-FEM simulation rationally explained the dislocation accumulation mechanism.

The CFD-FEM simulation has shown its rationality for the thermal stress distribution and evolution on the individual tracks with accurate temperature fields and few geometry simplifications. It should be mentioned that without incorporating accurate temperature-dependent thermal expansion coefficient and thermo-elastic-plastic constitutive relation, the current models are not able to provide accurate quantitative prediction of thermal stress. Moreover, the quantitative experimental measurement of thermal stress on individual tracks is also difficult, making the quantitative validation very challenging. Although some nice experimental measurement results of residual stresses have been reported by US national labs using X-ray [21] or neutron diffraction [57], such advanced large facilities are not accessible to us.

Due to the large computational cost, the CFD-FEM model faces difficulty to simulate the fabrication of a whole part. However, once the thermos-elastic-plastic constitutive law and the temperature-
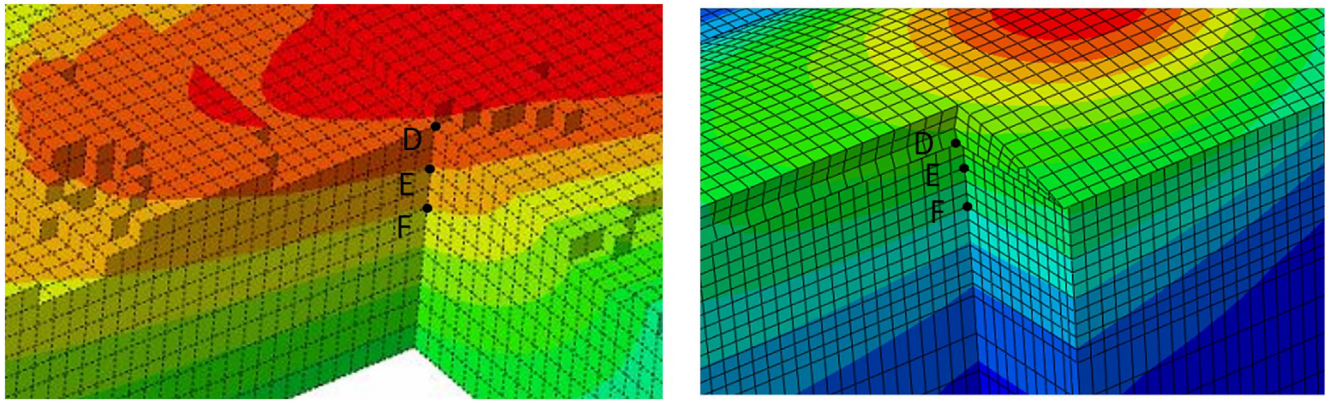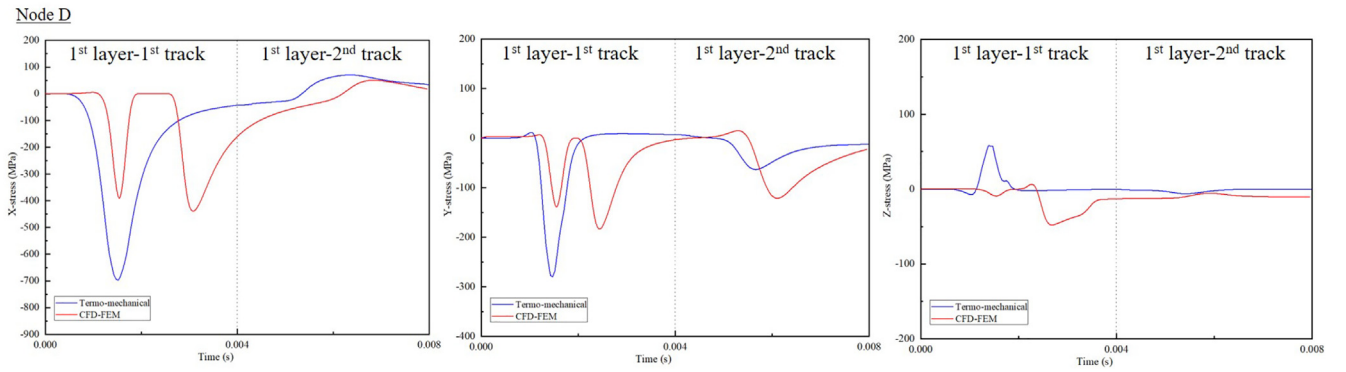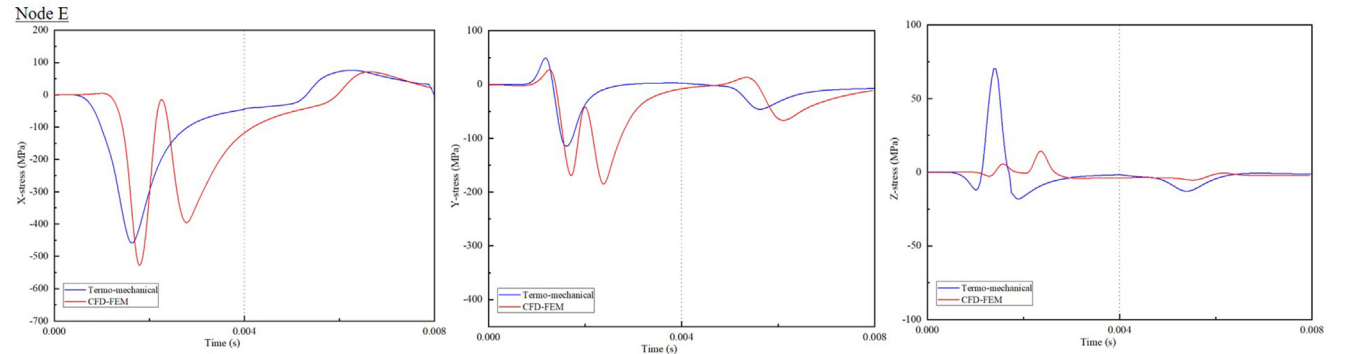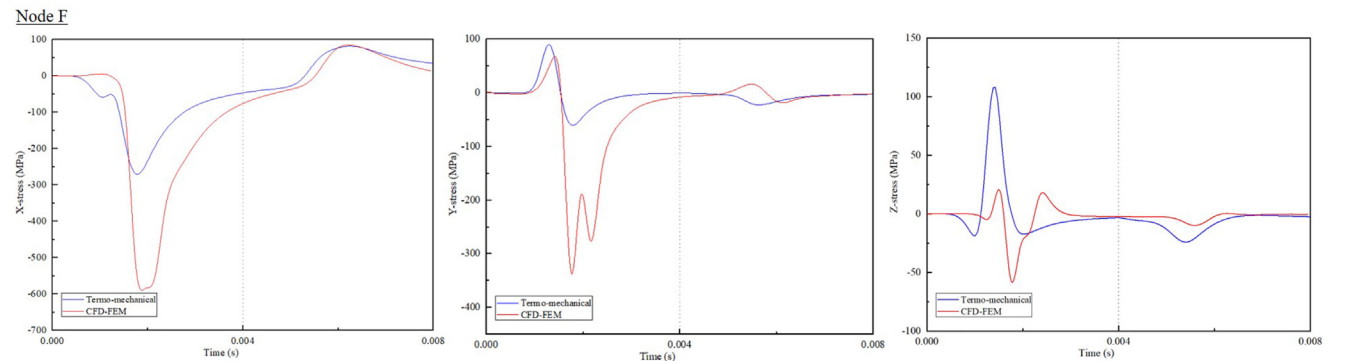
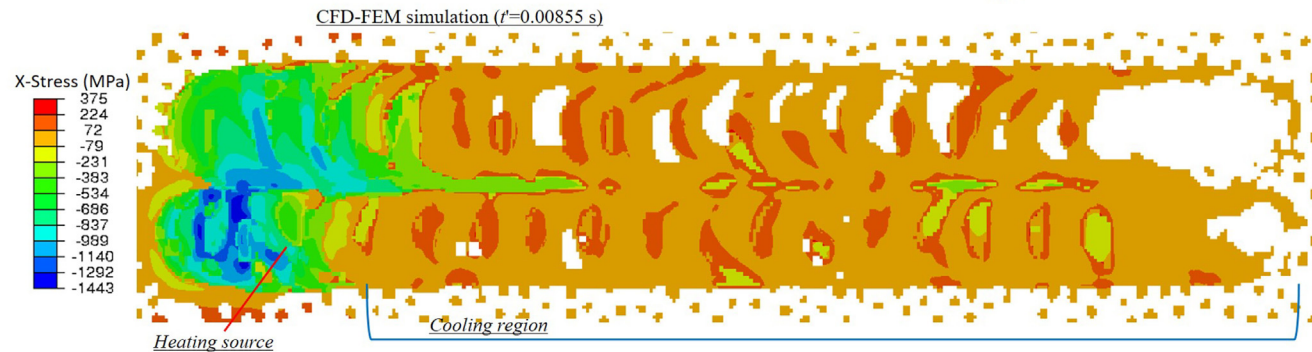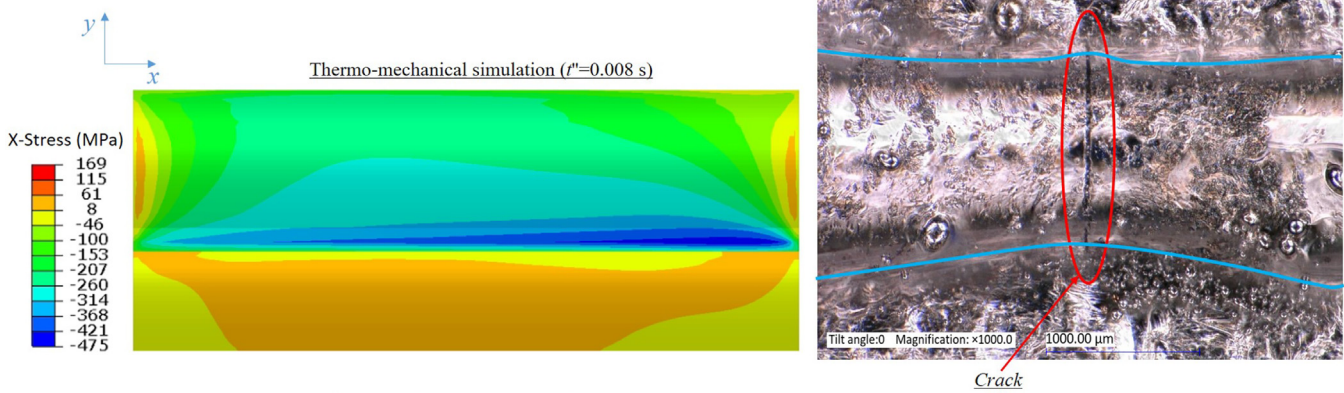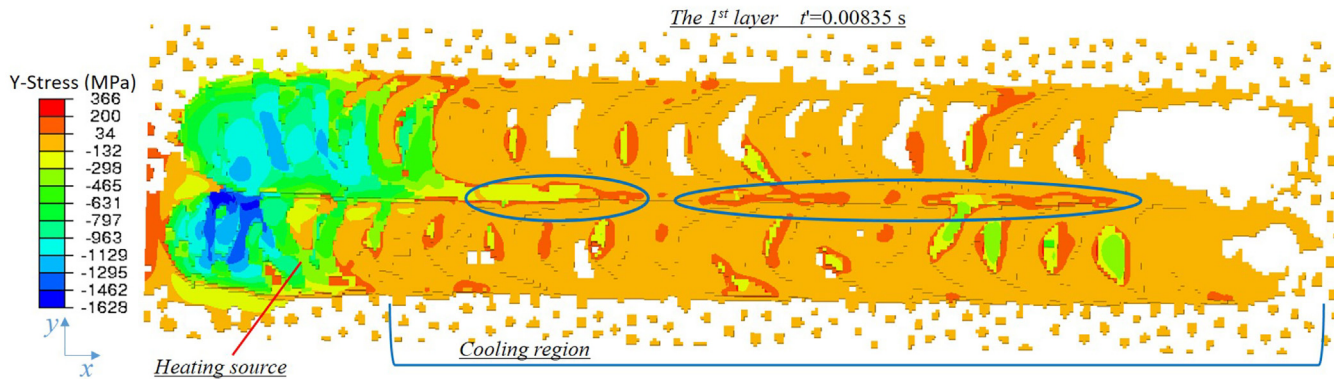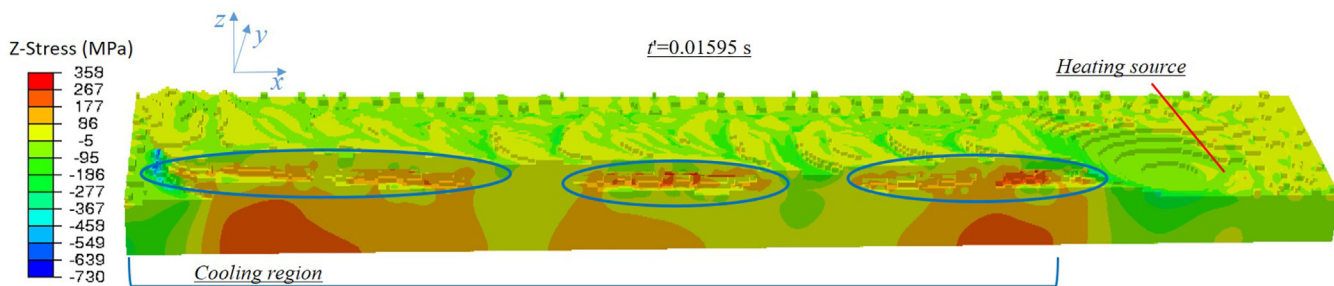**Fig. 11.** (a) Selected nodes, D, E and F, in the CFD-FEM and thermo-mechanical simulations. The stress component curves in x, y and z direction at 3 nodes, (b) D, (c) E, and (d) F.
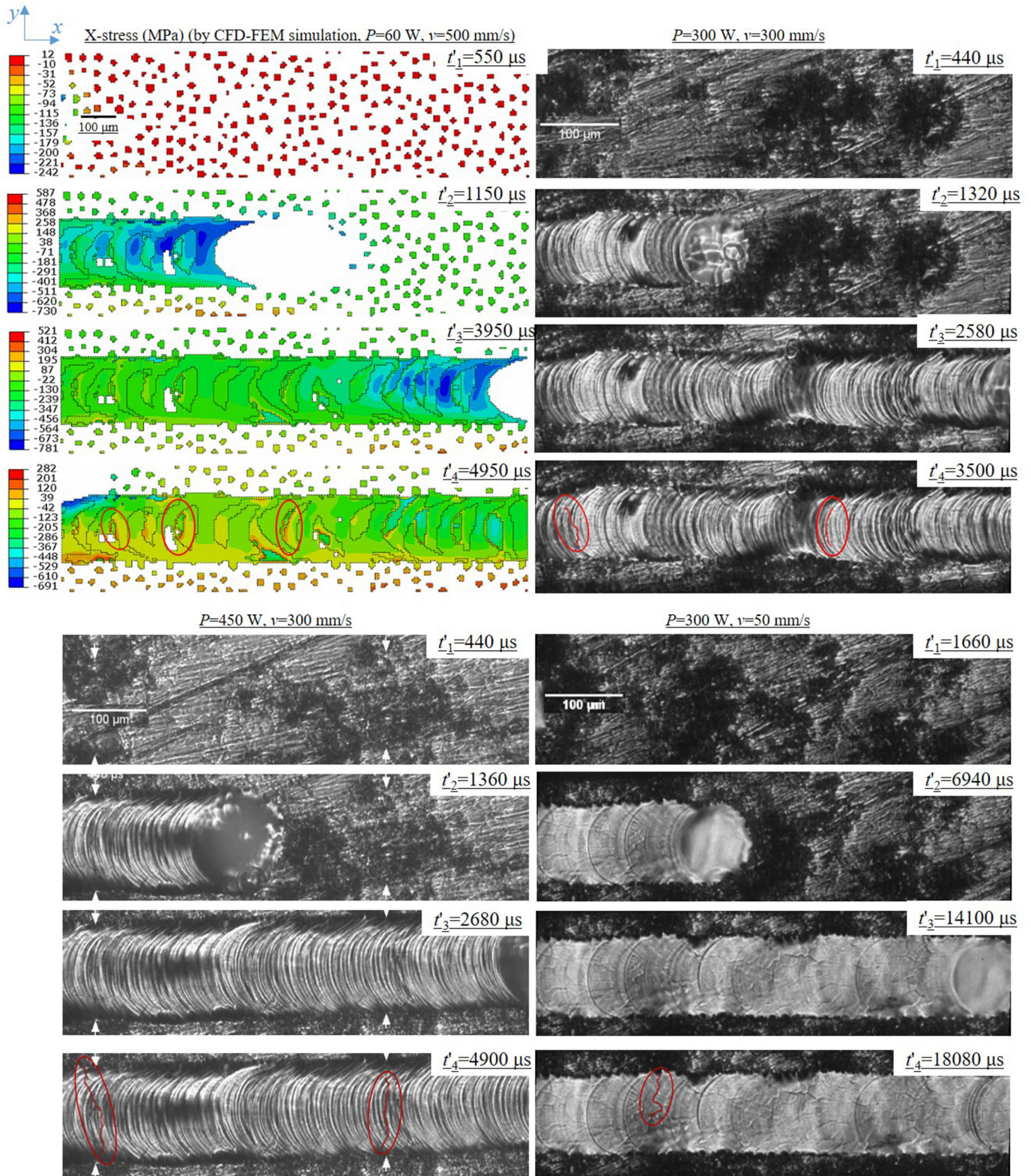
(a)

(b)

(c)

Fig. 12. (a) The crack occurring on the single-track sample; the X-stress distribution in the thermo-mechanical and CFD-FEM simulation at $t_1'' = 0.008s$, $t_1' = 0.00855s$, respectively; (b) the Y-stress distribution at $t_1' = 0.00835$ s; (c) the Z-stress distribution at $t_1' = 0.01595$ s.

Fig. 13. The evolution of the X-stress by CFD-FEM simulation compared with the observed cracking in the single track experiments [55]. (The experimental figures are reused under CC-BY 4.0 license.)

dependent material properties are accurately measured in experiments, the more accurate thermal strain and stress in melt tracks can be achieved. Subsequently, with proper multi-scale modelling approaches, e.g., macro-scale modelling of the sequential accumulation of melt tracks with the accurate thermal strains from this meso-scale CFD-FEM model, a whole part can be simulated in an efficient and accurate way, and the experimental validation in part scale can be further conducted.

5. Conclusion

A high-fidelity modelling approach for the thermal stress prediction of the powder bed fusion process has been constructed. At first, the thermal-fluid and mechanical models are linked by the temperature interpolation that maps the temperature profiles from the thermal-fluid model into the FEM model. Then, by loading the temperature instead of the heat flux, the FEM simulation is simplified as a pure mechanical analysis. Unlike the traditional thermo-mechanical applying the heat source directly on the predefined track surface, the temperature profiles of the thermal-fluid model have enabled the reappearance of the sophisticated physical phenomena of the melting procedure in the FEM model. Therefore, based on the quiet element method and the accurate temperature field, the defects such as the voids and the rough surface morphology have been revealed in the simulation results. Furthermore, as illustrated in the cross comparison with the thermo-mechanical model. With the consideration of the melting and re-melting procedure, the stress pattern for the CFD-FEM model in the molten pool region is more complicated; while in the unmelted region of the two methods, the trend of stress curves is similar but the magnitude differs. Finally, the overall stress distribution in the cooling region of the CFD-FEM model reveals the possible reasons for the generation of the cracks.

CRediT authorship contribution statement

Chen Fan: Methodology, Software, Validation, Formal analysis, Investigation, Data curation, Writing - original draft. **Wentao Yan:** Conceptualization, Methodology, Software, Resources, Writing - review & editing, Supervision, Project administration, Funding acquisition.

Declaration of Competing Interest

The authors declare that they have no known competing financial interests or personal relationships that could have appeared to influence the work reported in this paper.

Appendix A. Appendix

In Fig. 15, the first two tracks are formed during 0 ~ 0.008 s to be the first layer which is subsequently overlaid by the deposition of the rest two tracks during 0.008 ~ 0.016 s. Due to the different iterations of the two simulations, the displayed time frames for the results of the FEM simulation is 0.0005 s earlier than that of the thermal-fluid simulation. It reveals that the temperature field shows a remarkable agreement between two models in the whole deposition process of 4 tracks, and the FEM simulation manages to inherit the geometrical feature of the thermal-fluid model.
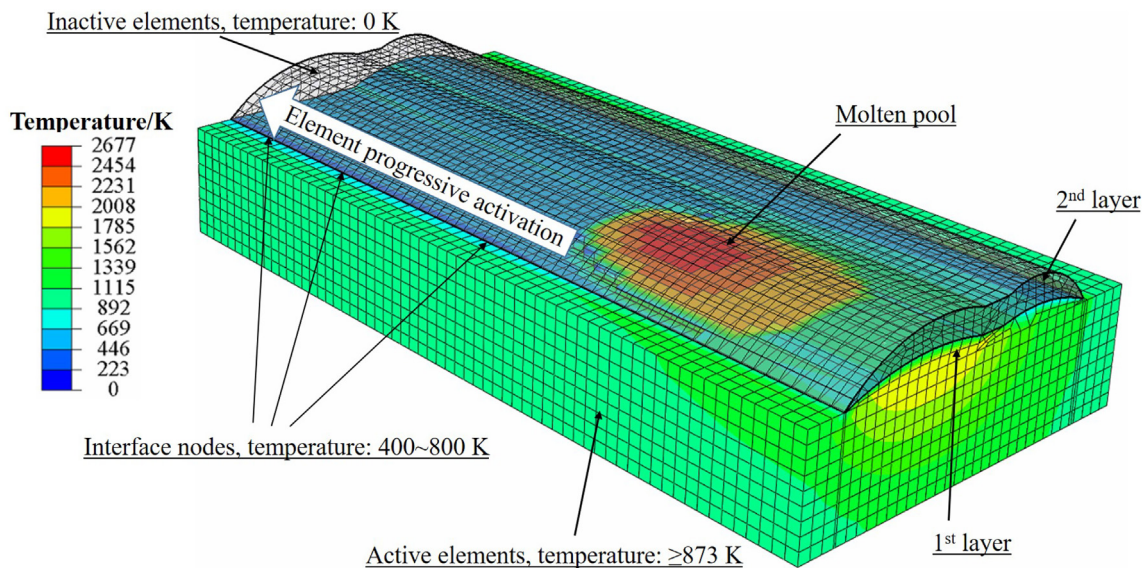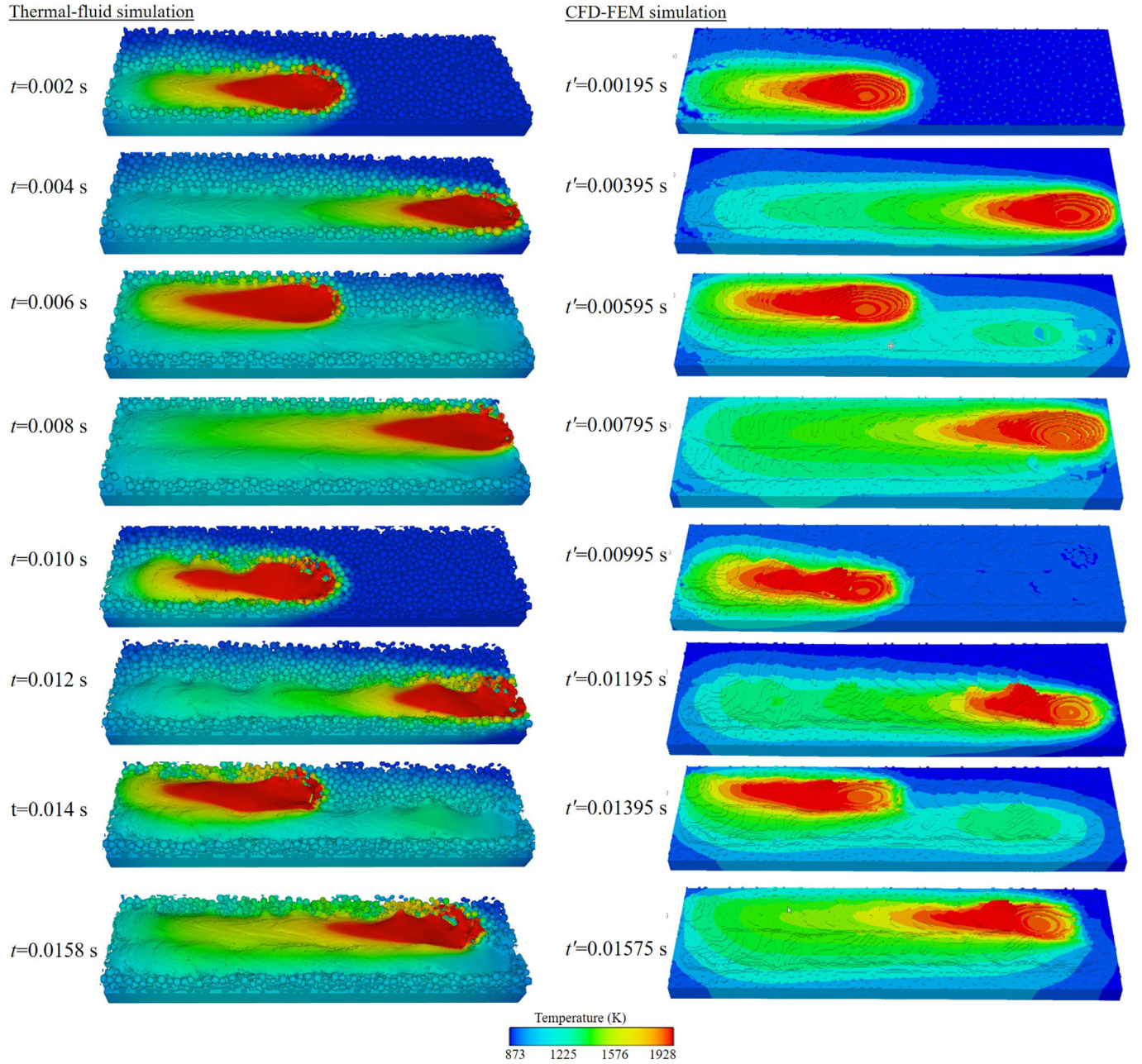

Fig. 14. Schematic of the inactive elements model and the relatively lower temperature on the interface nodes between inactive elements and active elements.

Fig. 15. The comparison of the simulation results between the FEM model and the CFD model within 4 heating intervals which denote the deposition process of the 1st-layer 1st-track during 0 ~ 0.004 s, the 1st-layer 2nd-track during 0.004 ~ 0.008 s, the 2nd-layer 1st-track during 0.008 ~ 0.012 s, and the 2nd-layer 2nd-track during 0.012 ~ 0.016 s, respectively.
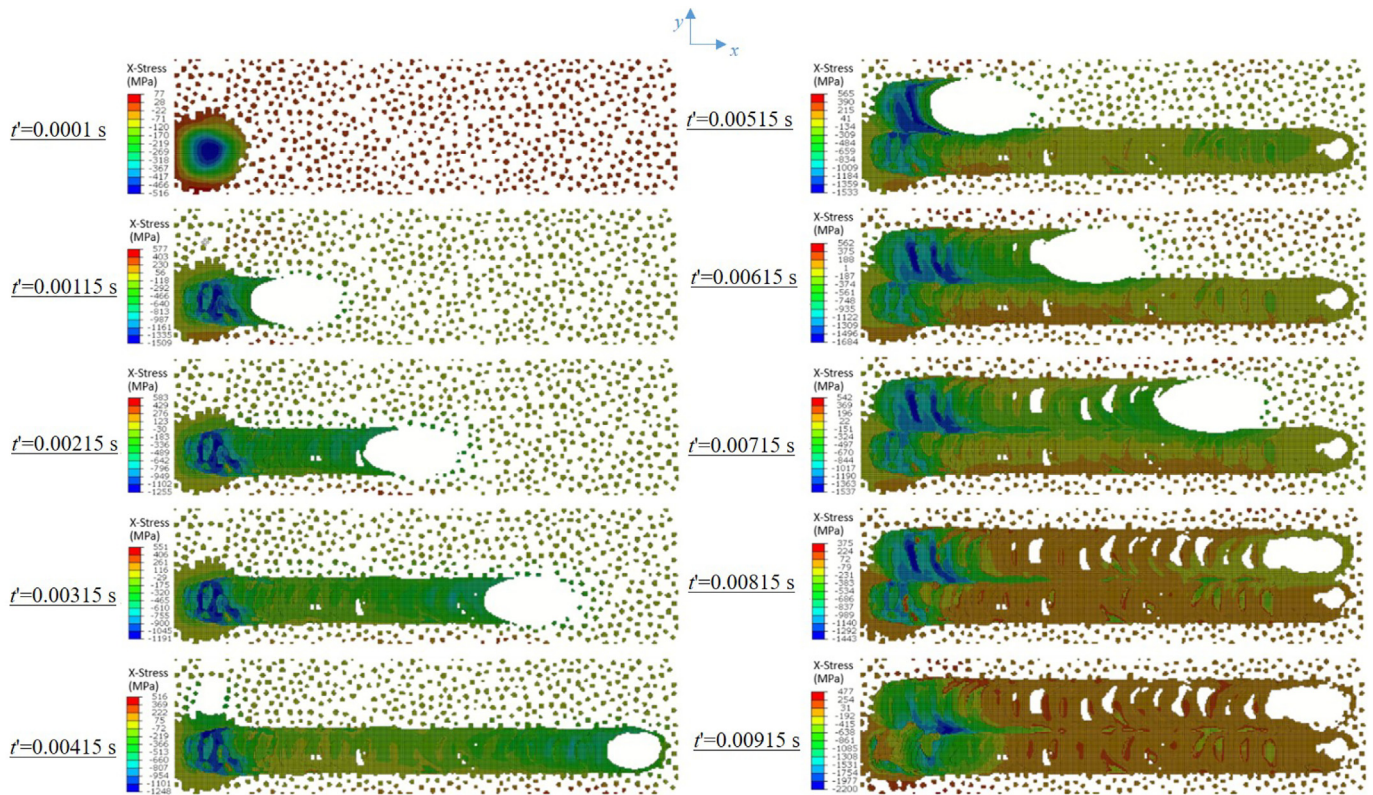
Fig. 16. Picture frames showing the evolution process of the X-stress distribution on the first layer.

References

[1] J. Smith, W. Xiong, W. Yan, S. Lin, P. Cheng, O.L. Kafka, G.J. Wagner, J. Cao, W.K. Liu, Linking process, structure, property, and performance for metal-based additive manufacturing: computational approaches with experimental support, Comput. Mech. 57 (4) (2016) 583–610.

[2] C. Li, Z. Liu, X. Fang, Y. Guo, Residual stress in metal additive manufacturing, Proc. Cirp 71 (2018) 348–353.

[3] E.R. Denlinger, J.C. Heigel, P. Michaleris, Residual stress and distortion modeling of electron beam direct manufacturing ti-6al-4v, Proc. Inst. Mech. Eng. B J. Eng. Manuf. 229 (10) (2015) 1803–1813.

[4] Y. Lu, S. Wu, Y. Gan, T. Huang, C. Yang, L. Junjie, J. Lin, Study on the microstructure, mechanical property and residual stress of slm inconel-718 alloy manufactured by differing island scanning strategy, Opt. Laser Technol. 75 (2015) 197–206.

[5] V. Cain, L. Thijs, J. Van Humbeeck, B. Van Hooreweder, R. Knutsen, Crack propagation and fracture toughness of ti6al4v alloy produced by selective laser melting, Addit. Manuf. 5 (2015) 68–76.

[6] N.J. Harrison, I. Todd, K. Mumtaz, Reduction of micro-cracking in nickel superalloys processed by selective laser melting: a fundamental alloy design approach, Acta Mater. 94 (2015) 59–68.

[7] A. Bauereiß, T. Scharowsky, C. Körner, Defect generation and propagation mechanism during additive manufacturing by selective beam melting, J. Mater. Process. Technol. 214 (11) (2014) 2522–2528.

[8] W. Yan, W. Ge, Y. Qian, S. Lin, B. Zhou, W.K. Liu, F. Lin, G.J. Wagner, Multi-physics modeling of single/multiple-track defect mechanisms in electron beam selective melting, Acta Mater. 134 (2017) 324–333.

[9] D. Peral, J. De Vicente, J. Porro, J. Ocana, Uncertainty analysis for non-uniform residual stresses determined by the hole drilling strain gauge method, Measurement 97 (2017) 51–63.

[10] A. Salmi, E. Atzeni, L. Iuliano, M. Galati, Experimental analysis of residual stresses on alsi10mg parts produced by means of selective laser melting (slm), Procedia CIRP 62 (2017) 458–463.

[11] P. Rangaswamy, M. Griffith, M. Prime, T. Holden, R. Rogge, J. Edwards, R. Sebring, Residual stresses in lens® components using neutron diffraction and contour method, Mater. Sci. Eng. A 399 (1–2) (2005) 72–83.

[12] B. Vrancken, V. Cain, R. Knutsen, J. Van Humbeeck, Residual stress via the contour method in compact tension specimens produced via selective laser melting, Scr. Mater. 87 (2014) 29–32.

[13] M. Kabiri, Nonuniform residual-stress measurement by hole-drilling method, Exp. Mech. 24 (4) (1984) 328–336.

[14] K. Zeng, D. Pal, H. Gong, N. Patil, B. Stucker, Comparison of 3dsim thermal modelling of selective laser melting using new dynamic meshing method to ansys, Mater. Sci. Technol. 31 (8) (2015) 945–956.

[15] L. Gasman, Additive aerospace considered as a business, Additive Manufacturing for the Aerospace Industry, Elsevier 2019, pp. 327–340.

[16] Y. Yang, M. Allen, T. London, V. Oancea, Residual strain predictions for a powder bed fusion inconel 625 single cantilever part, Integrating Mater. Manuf. Innov. 8 (3) (2019) 294–304.

[17] J. Heigel, P. Michaleris, E.W. Reutzel, Thermo-mechanical model development and validation of directed energy deposition additive manufacturing of ti–6al–4v, Addit. Manuf. 5 (2015) 9–19.

[18] E.R. Denlinger, P. Michaleris, Effect of stress relaxation on distortion in additive manufacturing process modeling, Addit. Manuf. 12 (2016) 51–59.

[19] X. Liang, L. Cheng, Q. Chen, Q. Yang, A. C. To, A modified method for estimating inherent strains from detailed process simulation for fast residual distortion prediction of single-walled structures fabricated by directed energy deposition, Addit. Manuf. 23 (2018) 471–486.

[20] X. Liang, Q. Chen, L. Cheng, D. Hayduke, A. C. To, Modified inherent strain method for efficient prediction of residual deformation in direct metal laser sintered components, Comput. Mech. 64 (6) (2019) 1719–1733.

[21] R. Ganeriwala, M. Strantza, W. King, B. Clausen, T.Q. Phan, L.E. Levine, D.W. Brown, N. Hodge, Evaluation of a thermomechanical model for prediction of residual stress during laser powder bed fusion of ti-6al-4v, Addit. Manuf. 27 (2019) 489–502.

[22] Y. Zhang, J. Zhang, Finite element simulation and experimental validation of distortion and cracking failure phenomena in direct metal laser sintering fabricated component, Addit. Manuf. 16 (2017) 49–57.

[23] P. Prabhakar, W.J. Sames, R. Dehoff, S.S. Babu, Computational modeling of residual stress formation during the electron beam melting process for inconel 718, Addit. Manuf. 7 (2015) 83–91.

[24] A. Hussein, L. Hao, C. Yan, R. Everson, Finite element simulation of the temperature and stress fields in single layers built without-support in selective laser melting, Mater. Des. 52 (2013) (1980-2015) 638–647.

[25] R. Xie, G. Chen, Y. Zhao, S. Zhang, W. Yan, X. Lin, Q. Shi, In-situ observation and numerical simulation on the transient strain and distortion prediction during additive manufacturing, J. Manuf. Process. 38 (2019) 494–501.

[26] X. Song, S. Feih, W. Zhai, C.-N. Sun, F. Li, R. Maiti, J. Wei, Y. Yang, V. Oancea, L.R. Brandt, et al., Advances in additive manufacturing process simulation: residual stresses and distortion predictions in complex metallic components, Mater. Des. 108779 (2020).

[27] P. Foteinopoulos, A. Papacharalampopoulos, K. Angelopoulos, P. Stavropoulos, Development of a simulation approach for laser powder bed fusion based on scanning strategy selection, Int. J. Adv. Manuf. Technol. 108 (9) (2020) 3085–3100.

[28] S.H. Nikam, N. Jain, Modeling and prediction of residual stresses in additive layer manufacturing by microplasma transferred arc process using finite element simulation, J. Manuf. Sci. Eng. 141 (6) (2019).

[29] M. Yi, B.-X. Xu, O. Gutfleisch, Computational study on microstructure evolution and magnetic property of laser additively manufactured magnetic materials, Comput. Mech. 64 (4) (2019) 917–935.

[30] R. Paul, S. Anand, F. Gerner, Effect of thermal deformation on part errors in metal powder based additive manufacturing processes, J. Manuf. Sci. Eng. 136 (3) (2014).

[31] W. Yan, W. Ge, J. Smith, S. Lin, O.L. Kafka, F. Lin, W.K. Liu, Multi-scale modeling of electron beam melting of functionally graded materials, Acta Mater. 115 (2016) 403–412.

[32] T. Mukherjee, W. Zhang, T. DebRoy, An improved prediction of residual stresses and distortion in additive manufacturing, Comput. Mater. Sci. 126 (2017) 360–372.

[33] J. Cheon, S.-J. Na, Prediction of welding residual stress with real-time phase transformation by cfd thermal analysis, Int. J. Mech. Sci. 131 (2017) 37–51.

[34] J. Cheon, D.V. Kiran, S.-J. Na, Cfd based visualization of the finger shaped evolution in the gas metal arc welding process, Int. J. Heat Mass Transf. 97 (2016) 1–14.

[35] J. Cheon, D.V. Kiran, S.-J. Na, Thermal metallurgical analysis of gma welded ah36 steel using cfd–fem framework, Mater. Des. 91 (2016) 230–241.

[36] N.S. Bailey, C. Katinas, Y.C. Shin, Laser direct deposition of aisi h13 tool steel powder with numerical modeling of solid phase transformation, hardness, and residual stresses, J. Mater. Process. Technol. 247 (2017) 223–233.

[37] P. Foteinopoulos, A. Papacharalampopoulos, P. Stavropoulos, On thermal modeling of additive manufacturing processes, CIRP J. Manuf. Sci. Technol. 20 (2018) 66–83.

[38] A. Lundbäck, L.-E. Lindgren, Modelling of metal deposition, Finite Elem. Anal. Des. 47 (10) (2011) 1169–1177.

[39] E.R. Denlinger, J. Irwin, P. Michaleris, Thermomechanical modeling of additive manufacturing large parts, J. Manuf. Sci. Eng. 136 (6) (2014).

[40] M. J. Dantin, W. M. Furr, M. W. Priddy, Towards an Open-Source, Preprocessing Framework for Simulating Material Deposition for a Directed Energy Deposition Process.

[41] A. Krishnakumar, K. Suresh, A. Chandrasekar, Towards Assembly-Free Methods for Additive Manufacturing Simulation, in: ASME 2015 International Design Engineering Technical Conferences and Computers and Information in Engineering Conference, American Society of Mechanical Engineers Digital Collection 2015.

[42] H. Huang, N. Ma, J. Chen, Z. Feng, H. Murakawa, Toward large-scale simulation of residual stress and distortion in wire and arc additive manufacturing, Addit. Manuf. (2020) 101248.

[43] P. Michaleris, Modeling metal deposition in heat transfer analyses of additive manufacturing processes, Finite Elem. Anal. Des. 86 (2014) 51–60.

[44] W. Yan, S. Lin, O.L. Kafka, Y. Lian, C. Yu, Z. Liu, J. Yan, S. Wolff, H. Wu, E. Ndip-Agbor, et al., Data-driven multi-scale multi-physics models to derive process–structure–property relationships for additive manufacturing, Comput. Mech. 61 (5) (2018) 521–541.

[45] T.K. Ales, An Integrated Model for the Probabilistic Prediction of Yield Strength in Electron-Beam Additively Manufactured Ti-6al-4v, 2018.

[46] L.-E. Lindgren, E. Hedblom, Modelling of addition of filler material in large deformation analysis of multipass welding, Commun. Numer. Methods Eng. 17 (9) (2001) 647–657.

[47] W. Yan, Y. Qian, W. Ge, S. Lin, W.K. Liu, F. Lin, G.J. Wagner, Meso-scale modeling of multiple-layer fabrication process in selective laser melting: inter-layer/track voids formation, Mater. Des. 141 (2018) 210–219.

[48] S.M.H. Hojjatzadeh, N.D. Parab, W. Yan, Q. Guo, L. Xiong, C. Zhao, M. Qu, L.I. Escano, X. Xiao, K. Fezzaa, et al., Pore elimination mechanisms during 3d printing of metals, Nat. Commun. 10 (1) (2019) 1–8.

[49] C.W. Hirt, B.D. Nichols, Volume of fluid (vof) method for the dynamics of free boundaries, J. Comput. Phys. 39 (1) (1981) 201–225.

[50] B. Cheng, S. Shrestha, K. Chou, Stress and deformation evaluations of scanning strategy effect in selective laser melting, Addit. Manuf. 12 (2016) 240–251.

[51] D. Dassault Systèmes, Abaqus Analysis User's Guide, Tech. rep., Technical Report Abaqus 6.14 Documentation Simulia Corp, 2016.

[52] J.N. Reddy, An Introduction to the Finite Element Method, New York 27, 1993.

[53] I. Yadroitsev, I. Yadroitsava, Evaluation of residual stress in stainless steel 316l and ti6al4v samples produced by selective laser melting, Virtual Phys. Prototy. 10 (2) (2015) 67–76.

[54] B. Vrancken, R. Wauthlé, J.-P. Kruth, J. Van Humbeeck, Study of the influence of material properties on residual stress in selective laser melting, Proceedings of the Solid Freeform Fabrication Symposium 2013, pp. 393–407.

[55] B. Vrancken, R.K. Ganeriwala, M.J. Matthews, Analysis of laser-induced microcracking in tungsten under additive manufacturing conditions: experiment and simulation, Acta Mater. (2020) 464–472.

[56] G. Wang, H. Ouyang, C. Fan, Q. Guo, Z. Li, W. Yan, Z. Li, The origin of high-density dislocations in additively manufactured metals, Mater. Res. Lett. 8 (8) (2020) 283–290.

[57] K. An, L. Yuan, L. Dial, I. Spinelli, A.D. Stoica, Y. Gao, Neutron residual stress measurement and numerical modeling in a curved thin-walled structure by laser powder bed fusion additive manufacturing, Mater. Des. 135 (2017) 122–132.